Volume 22, No 2 | International Journal of Radiation Research, April 2024

# The effect of MATLAB-based metal artifact reduction software on radiotherapy dose distribution

**A. Inal[1*] and S. Barlaz Us[2]**

[1]*Department of Radiation Oncology, Health of Science University, Antalya Training and Research Hospital, Kazım Karabekir Street, Muratpaşa, Antalya, Turkey*

[2]*Department of Radiation Oncology, Mersin University School of Medicine Department, Çiftlikköy Kampüsü, Yenişehir, Mersin, Turkey*

► ***Original article***

***Corresponding author:***
*Aysun Inal, Ph.D.,*
***E-mail:*** *aysuntoy@yahoo.com*

**Received:** February 2023
**Final revised:** November 2023
**Accepted:** November 2023

***Int. J. Radiat. Res., April 2024; 22(2): 367-372***

**DOI:** 10.61186/ijrr.22.2.3367

***Keywords:*** *Metal artifact reduction, radiotherapy, gamma analysis, MATLAB.*

## ABSTRACT

***Background***: Metal Artifact Reduction (MAR) is very important in terms of dose calculation and optimization accuracy in radiotherapy (RT). There are many MAR programs available commercially. In this study, a MAR program was developed using MATLAB software (MATLAB-MAR), and the effect of the developed MATLAB-MAR on radiotherapy dose distribution was examined. ***Materials and Methods:*** In line with the purpose of the study, a phantom containing metal with a high atomic number (z=82) was created, and computer tomography (CT) of the phantom was taken. MAR developed with MATLAB software and a commercial metal artifact reduction (Smart-MAR) were applied on CT slices. The Hounsfield unit (HU), visually, artefact size and gamma evaluation effects of MATLAB-MAR, Smart-MAR and Without-MAR slices in the CMS XiO planning systems. ***Results:*** As a result of the study, the best visually and HU improvement was seen in MATLAB-MAR. Moreover, in the dose distribution evaluation made by gamma analysis, an improvement was observed in MATLAB-MAR. ***Conclusion:*** Although similar values were obtained with MATLAB-MAR and the commercial software, it was determined that MATLAB-MAR was more advantageous than the commercial software in terms of being cost-free, providing results in a shorter time, not requiring reconstruction, and being open to development.

## INTRODUCTION

In radiotherapy, for the delineation of tumors and organs at risk, the computed tomography (CT) data are used in combination with other imaging methods [1, 2]. The CT is also utilized as the basis for calculating the patient dose distributions [3]. During the CT imaging process, high-density materials such as hip replacement implants, dental fillings, or surgical clips can cause metal artifacts [4]. In addition, a combination of mechanisms such as photon starvation, beam hardening, scattering, and partial volume effects also leads to metal artifacts [5]. Because of the polychromatic nature of x-ray beams, beam hardening occurs in CT systems. In addition, due to the hardening and scatter of the beam, dark streaks are formed [6, 7]. This situation causes difficulties in the identification of anatomical structures in CT images and leads to changes in the CT numbers, which is called Hounsfield Unit (HU) of the structures, due to missing data [8]. Inaccuracies in the HU values cause an error in the electron density or stopping power estimation. This error significantly affects the dose calculation and optimization processes [9, 10]. This is a dosimetric problem that may cause inaccuracies in the evaluation of the dose distribution of the patient to be treated.

Various Metal Artifact Reduction (MAR) algorithms have been developed to reduce metal artifacts [11]. One of them is the iterative MAR algorithm [12]. Some MAR methods includes interpolation-based sonogram correction, non-interpolation-based sonogram correction, hybrid sonogram correction, iterative image reconstruction, and image-based approaches [11]. Generally, in MAR methods, the projections passing through a metal section in patient data are replaced with interpolated data obtained from neighboring projections [13]. Because of the CT images disrupted by metal artifacts, many studies have been conducted to investigate the effects of metal artifacts on CT images in radiation therapy [14-16]. Performances of various MAR algorithms have been usually assessed in terms of their ability to improve accurate anatomical structure definition and dose calculation for RT. Some studies have revealed that commercial MAR algorithms play a significant role in reducing the metal artifact effect and improving dose calculation accuracy [17, 18].

In this study, we developed an alternative MAR algorithm, called MATLAB-MAR, by using the MATLAB program (R2016a, USA) to eliminate this dosimetric problem without utilizing a commercial MAR algorithm. In the context of the study, the

[ Downloaded from ijrr.com on 2026-11-22 ]

[ DOI: 10.61186/ijrr.22.2.367 ]

developed algorithm was compared with commercial MAR (Smart-MAR) software in terms of Hounsfield artifact size, Hounsfield unit, visual, and gamma passing rate (GPR).

## MATERIALS AND METHODS

### *Phantom arrangement and CT procedures*

In the context of the study, a number of works have been conducted in order to investigate the accuracy of the developed MATLAB-Mar software on the artifact effects of metal with a high atomic number. For the arrangement of phantoms, two 5 mm bolus materials were placed on top of the 50 mm water equivalent solid phantom (SP34 white polystyrene IBA Dosimetry GmbH, Germany). Metals, which had dimensions of 31 × 31 × 2 mm (left) and 31 × 31 × 2 mm (right), were placed between two boluses and 20 mm beyond the phantom edge (figure 1). Then, 50 mm solid phantoms were placed on the bolus. The schematic representation of the phantom arrangement from the top (a) and front (b) views is given in figure1.

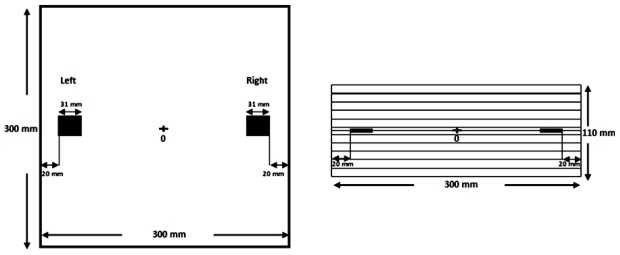



**Figure 1.** Schematic representation of the top view of the phantom arrangement **(a)** (Lateral axis: x axis (300 mm), vertical axis: y axis (300mm). The square geometric shape in black represents the metal objects with a side length of 31 mm. Schematic arepresentation of the front view of the phantom arrangement **(b)**. (Lateral axis: x axis, vertical axis: z axis) The square geometric shape in black represents metal objects with a side edge length of 31 mm and a thickness of about 2 mm.

Axial images of this phantom were obtained at a slice thickness of 0.625 mm and 120 kVp tube voltage on CT (General Electric Healthcare, Chicago, IL, USA). These images obtained from CT were considered to be the original set with metal effect without MAR correction (Without-MAR (WM)). On these CT images, two corrected image sets were created by using both the commercial MAR algorithm (Smart-MAR (SM)) and the MATLAB-MAR (MM) software developed in the MATLAB environment. All dosimetric comparisons were carried out for these three different sets of images. The extended CT-scale application was not used, and the metal HU value was fixed as 3071.

### *Performing corrections on the original CT images by using the developed MATLAB-MAR software*

In this study, an in-house software was developed by using the MATLAB computer program to be able to correct CT images effectively. Before starting the image processing, CT images (Without-MAR) of the phantom were transferred to the computer in DICOM format. For the transformation process, the first step is image segmentation. Image segmentation can be described as the division of images into regions corresponding to the structure of interest. To achieve the image segmentation process, the maximum HU value (Metals HU value) is determined first in the entire image, and this value is assigned as the threshold value. In this study also, the segmentation of the CT images was performed based on the determined threshold value (HU value of metal). Then, using MATLAB Image Processing Toolbox, artifact image maps, called scattering patterns showing the scattering caused by high-density structures, were created (figure 2 (a)). Patterns of the high-density structures such as couch (other patterns), except for the metal structure that creates artifacts in the image, were removed from the scattering pattern, and the image of the main pattern was obtained (figure 2. (b), (c)).

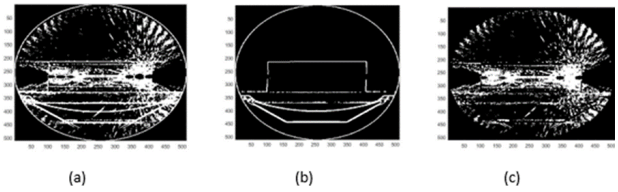



**Figure 2.** The scattering pattern caused by high-density structures **(a)**. The pattern of high-density structures other than metal **(b)**. The main pattern obtained by removing the other patterns from the scattering pattern **(c)**. Lateral axis: x axis, vertical axis: z axis)

The second step of the transformation process is the application of the median filter. The median filter not only helps to reduce noise and smooth the signal but also preserves sharp details. It is a nonlinear filter that is available as standard in the MATLAB toolbox. However, when the median filter in the MATLAB toolbox is applied to the entire image, it causes all HU values in the image to change. Therefore, the median filter should only be applied to the area where the artifact is dense. In this context, median filter codes were rewritten to make field limitations on the scattering pattern, and in this way, the in-house MAR software was developed. Then, the rewritten median filter code was applied to original CT slices. Finally, CT images corrected using the MAR software developed in the MATLAB program were obtained in DICOM format. In the context of this study, CT images corrected by the developed in-house MAR software were called MATLAB-MAR (MM).

[ Downloaded from ijrr.com on 2026-11-22 ]

[ DOI: 10.61186/ijrr.22.2.367 ]

***Procedures in the treatment planning systems (TPS)***

Before the mentioned phantom arrangement, the HU values and standard deviations of the water equivalent solid water phantom and bolus materials used in the study were found. The mean HU values were obtained along circles with a 10 and 30 - pixel - diameter (mm) region of interest, whose center was defined in the same coordinate metal-free phantom [figure (3a)], and which extended laterally from both metal edges in transverse slices for WM, SM and MM images (figure 3(b)).

CT images were transferred to the CMS XiO (CMS Co., St. Louis, MO, USA) treatment planning systems (TPSs). The treatment plans were calculated on WM, SM, and MM images by using 6 MV photon energy, superposition algorithm/step & shoot in CMS XiO. Five different treatment plans were obtained by using the Intensity Modulated Radiation Therapy (IMRT) technique for the linear accelerator device. The dose distributions on the WM, SM, and MM transverse and coronal slices were calculated in CMS XiO, and they were compared with each other (WM-SM, WM-MM, and SM-MM). The differences in dose distributions in the transverse and coronal planes were evaluated using the gamma passing rate (GPR) in the OmniProI'mRT software. (IBA Dosimetry, Schwarzenbruck, Germany). In this study, the GPR ($\gamma<1$) was performed based on $\Delta D$ = 1% (dose difference parameter) and $\Delta d$ = 1 mm (distance to agreement parameter) criteria.

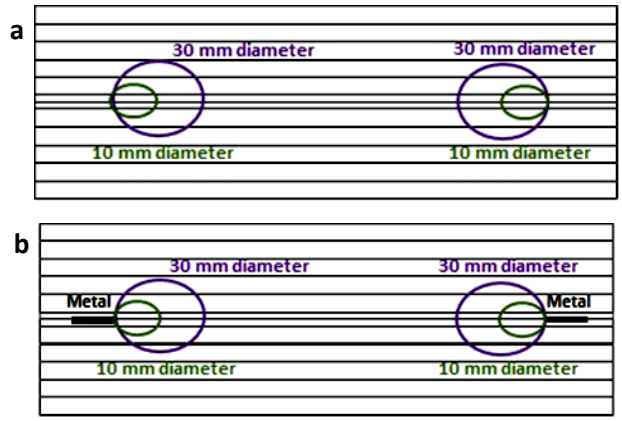



**Figure 3.** Regions where HU values are obtained in the phantom. Circles with diameter of 10 and 30 mm, whose center was defined in the same coordinate metal-free phantom **(a)**, and with metal phantom **(b)**. WM: Without MAR, SM: Smart MAR, MM: MATLAB-MAR (Lateral axis: x axis, vertical axis: z axis).

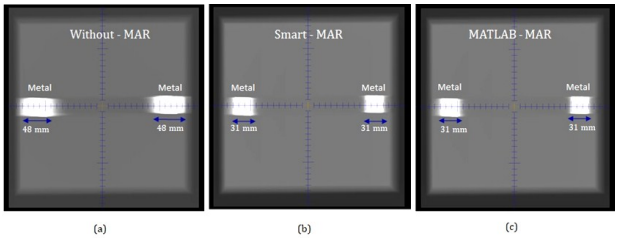



**Figure 4.** The Digitally Reconstructed Radiographs (DRR) images for WM **(a)**, SM **(b)**, and MM **(c)**. (Lateral axis: x axis, vertical axis: y axis). The white geometric shape represents the changing size of CT images of the square metal object, which actually has a side length of 31 mm. WM: Without MAR, SM: Smart MAR, MM: MATLAB-MAR.

## RESULTS

***Size and visual evaluation***

The results of this study revealed that metal sizes in the coronal axis of the original images (WM) appeared clearly larger than the actual size (figure 4). The right metal was measured approximately 51 mm, while the left metal was measured 48 mm. In both SM and MM images, it was seen (31mm) that the metals were in their real size (figure 4(b) and figure 4(c)).

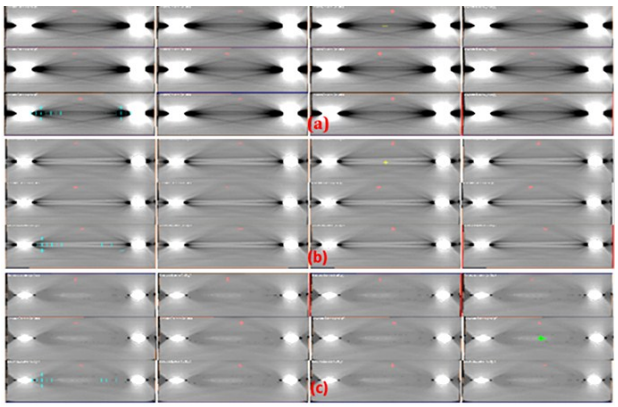



**Figure 5. (a), (b),** and **(c)** show images with the same window width (3000) and length (300) for WM, SM, and MM in the transverse axis, respectively. As seen, there are dark lines between right and left metals in the WM image (figure 5(a)). On the other hand, both the dark lines towards the lateral and the brightness around the metal are considerably reduced in the MM image (figure 5 (c)).

[ Downloaded from ijrr.com on 2026-11-22 ]

[ DOI: 10.61186/ijrr.22.2.367 ]

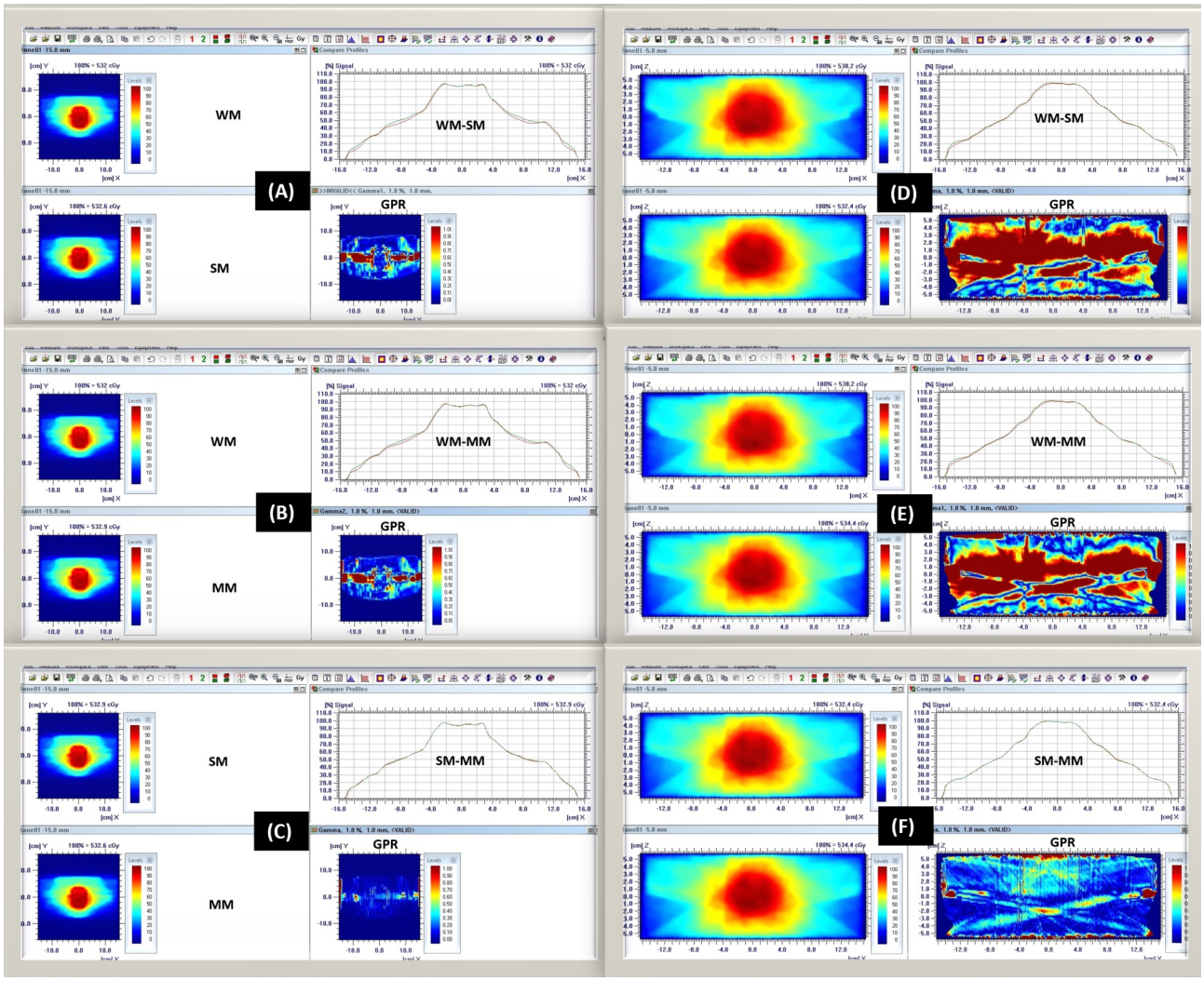



**Figure 6.** Coronal plane images of dose distributions, profile curves, GPMs, and comparisons with each other for WM-SM **(a)**, WM-MM **(b)**, and SM-MM **(c)**. (Lateral axis: x axis, vertical axis: y axis). Transverse plane images of dose distributions, profile curves, GPMs, and comparisons with each other for WM-SM **(d)**, WM-MM **(e)**, and SM-MM **(f)**. (Lateral axis: x axis, vertical axis: z axis). The points where the gamma evaluation failed are shown in red.

### *HU Evaluation*

The mean HU values and standard deviations of the metal-free water-equivalent and metal-containing phantom arrangements are shown in table 1. It is seen that the mean HU value increases while the radius of the circle area on the edge of the metals decreases.

**Table 1.** The HU values and standard deviations of the circle regions

| | | Circle Radius | | | |
|---|---|---|---|---|---|
| **Without Metal** | | 30 mm | | | |
| | | HU | | 10 mm | |
| | | Solid Phantom | SD | HU | SD |
| **Without Metal** | Bolus Material | 5 | ±3 | 4 | ±3 |
| **With Metal** | WMright | -6 | ±4 | -1 | ±5 |
| **With Metal** | SMright | -369 | ±362 | -918 | ±244 |
| | MMright | -131 | ±116 | -245 | ±189 |
| | WMleft | -96 | ±85 | -156 | ±120 |
| | SMleft | -247 | ±191 | -760 | ±409 |
| | MMleft | -104 | ±89 | -222 | ±195 |

### *GPR evaluation*

Table 2 shows the GPR between the WM and SM, WM and MM, and SM and MM dose maps of each plan (Plan I-Plan V) obtained on coronal and transverse slices on TPS. The fact that GPR differences between MAR applied and unapplied depth-dependent dose variation of the metal-containing region in both planes are greater indicates that remarkable images are seen, although the larger increase in the transverse plane.

**Table 2.** The GPR and mean values between the WM-SM, WM -MM, and SM-MM dose maps of each plan obtained on coronal and transverse slices on TPS. WM: Without MAR, SM: Smart MAR, MM: MATLAB-MAR

| | | Gamma passing rates (%) | | | | | |
|---|---|---|---|---|---|---|---|
| | | **Plan I** | **Plan II** | **Plan III** | **Plan IV** | **Plan V** | **Mean** |
| **Coronal Slices** | WM-SM | 88,35 | 89,24 | 88,57 | 88,62 | 91,19 | 89,19 |
| | WM-MM | 89,23 | 89,69 | 88,60 | 88,63 | 91,36 | 89,50 |
| | SM-MM | 96,94 | 98,63 | 97,97 | 97,95 | 97,66 | 97,83 |
| **Transverse Slices** | WM-SM | 68,41 | 62,51 | 73,68 | 71,45 | 74,45 | 70,10 |
| | WM-MM | 67,47 | 66,45 | 72,71 | 73,27 | 74,56 | 70,89 |
| | SM-MM | 96,14 | 96,27 | 95,81 | 96,08 | 96,34 | 96,13 |

[ Downloaded from ijrr.com on 2026-11-22 ]

[ DOI: 10.61186/ijrr.22.2.367 ]

For WM-SM (a), WM-MM (b), and SM-MM (c) treatment plans, the dose distributions, profile curves in which the two plans are compared, and gamma passing maps (GPM) are presented on the coronal plane in figure 6. In addition, dose distributions, profile curves, and gamma passing maps in the transverse plane are also presented for WM-SM, WM-MM, and SM-MM in figure 6 (d), (e), and (f), respectively. As seen in Figure 6, the red regions in the gamma passing maps indicate that the dose differences are higher than the acceptance value ($\gamma \geq 1$).

## DISCUSSION

In this study, although the commercial MAR algorithm provided a highly improved dataset, some residual artifacts were still observed in the corrected images. Similar observation was also reported by other studies [19, 20]. On the other hand, it was found that the MM tended to reduce the residues in the improved images a little more. It was observed that in the WM images, HU was significantly affected by metal artifacts. Jarriault and Lanaspeze found that HU errors were close to 20% for titanium hip replacement and 50% for steel hip replacement [21]. In the same study, the correction was performed with the commercial MAR software, and the mean HU values of metal-containing CT images and non-metal-containing CT images were compared. They reported that the results varied by 2%. In the present study, it was determined that the biggest differences between WM and MM mean HU values were 762 (-918 and -156) and 273 (-369 and -96) within the 10mm and 30mm circles, respectively. In their study, Katsura *et al.* reported that projection-based commercial MAR algorithms had quite positive effects on the correction of HU values [22]. In the current study, we also showed that photon starvation became more pronounced in metals with higher atomic numbers; however, both the SM and MM algorithm still had the same positive effect on CT images containing metal.

Spedea *et al.* noticed that the effect of MAR on dosimetry depended on the atomic number of the metal [15]. They reported that whereas low Z materials, such as titanium (Z = 22), did not produce significant dose errors, high Z materials, such as platinum (Z = 78), could substantially affect the dose calculation. They also found that the maximum dose difference of high Z material was 20%-25% in the region surrounding the metal [15]. In the present study, to be able to assess the dose calculation accuracy, the dose distributions for transverse and coronal slices were evaluated using a gamma analysis. As a result of the gamma analysis, it was observed that the dose distribution using both SM and MM was significantly improved compared to that of the uncorrected images (WM).

The results of MM software, which also reduces the increased patient dose in CT images taken by applying the MAR algorithm, revealed the success of the developed method. On the other hand, the fact that MM software was not tested on real patients' CT images containing prostheses can be shown as the limitation of this study. The next step of this study will be to investigate this limitation.

## CONCLUSION

The advantages of the MM under conditions of sufficient complementary information include the successful reduction of metal artifacts in reconstructed images. Although the MAR-corrected CT scan requires extra time and cost, the developed MM can reduce the time required for CT and it is cost-free. In addition, to be able to perform MAR correction on CT in the pelvic radiotherapy of patients with hip-prosthetics, this software is upgradeable.

**ACKNOWLEDGMENT**

*None.*

***Funding*:** No funding has been received for this study.

***Conflicts of interest statement*:** The authors had no conflicts of interest to declare.

***Author contributions*:** Concepts, design, literature search, experimental studies, manuscript preparation: A.I. , Data acquisition, Manuscript editing and manuscript review: A.I. & S.B.U.

## REFERENCES

1. Rousselle A, Amelot A, Thariat J, *et al.* (2020) Metallic implants and CT artefacts in the CTV area: Where are we in 2020? *Cancer Radiother*, ***24****(6-7): 658-666*.
2. Maerz M., Koelbl O, Dobler B (2015) Influence of metallic dental implants and metal artefacts on dose calculation accuracy. *Strahlentherapie und Onkologie, **191**: 234–241*.
3. Chu JC, Ni B, Kriz R, *et al.* (2000) Applications of simulator computed tomography number for photon dose calculations during radiotherapy treatment planning. *Radiotherapy and Oncology, **55:** 65–73*.
4. Huang V and Kohli K (2017) Evaluation of new commercially available metal artifact reduction (MAR) algorithm on both image quality and relative dosimetry for patients with hip prosthesis or dental fillings. *International Journal of Medical Physics, Clinical Engineering and Radiation Oncology, **5**(7): 124-138*.
5. De Man B, Nuyts J, Dupont P, *et al.* (1999) Metal streak artifacts in X-ray computed tomography: a simulation study. *IEEE Transactions on Nuclear Science, **46**(3): 691–696*.
6. Puvanasunthararajah S, Camps SM, Wille Ml *et al.* (2022) Combined clustered scan-based metal artifact reduction algorithm (CCS-MAR) for ultrasound-guided cardiac radioablation. *Phys Eng Sci Med*, ***45****: 1273–1287*.
7. Boas FE and Fleischmann D (2011) Evaluation of two iterative techniques for reducing metal artifacts in computed tomography. *Radiology, **259**: 894-902*.
8. Bar E, Schwahofer A, Kuchenbecker S, Harring P (2011) Improving radiotherapy planning in patients with metallic implants using the iterative metal artifact reduction (iMAR) algorithm. *Biomedical*

[ Downloaded from ijrr.com on 2026-11-22 ]

[ DOI: 10.61186/ijrr.22.2.367 ]

*Physics Engineering Express, **1**: 025206*.
9. Bedford JL, Childs PJ, Nordmark Hansen V, *et al.* (2003) Commissioning and quality assurance of the Pinnacle3 radiotherapy treatment planning system for external beam photons. *The British Journal of Radiology, **76**: 163–76*.
10. Kim Y, Tome WA, Bal M, McNutt TR, Spies L (2006) The impact of dental metal artefacts on head and neck IMRT dose distributions. *Radiotherapy and Oncology, **79**: 198–202*.
11. Abdoli M, Dierckx, RA, Zaidi H. Metal artifact reduction strategies for improved attenuation correction in hybrid PET/CT imaging. *Medical Physics* 39: 3343–3360; 2012.
12. Lell MM, Meyer E, Schmid M, *et al.* (2013) Frequency split metal artefact reduction in pelvic computed tomography. *European Journal of Radiology, **23**: 2137–45*.
13. Gjesteby L, De Man B, Jin Y, *et al.* (2016) Metal artifact reduction in CT: where are we after four decades? *IEEE Access, **4**: 5826–49*.
14. Giantsoudi D, De Man B, Verburg J, *et al.* (2017) Metal artifacts in computed tomography for radiation therapy planning: dosimetric effects and impact of metal artifact reduction. *Physics in Medicine & Biology, **62**(8): 49–80*.
15. Spadea MF, Verburg JM, Baroni G, Seco J (2014) The impact of low - Z and high - Z metal implants in IMRT: a Monte Carlo study of dose inaccuracies in commercial dose algorithms. *Medical Physics, **41**: 011702*.
16. Mail N, Albarakati Y, Khan MA, *et al.* (2013) The impacts of dental filling materials on RapidArc treatment planning and dose delivery: challenges and solution. *Medical Physics, **40**(8): 081714*.
17. Morsbach F, Bickelhaupt S, Wanner GA, *et al.* (2013) Reduction of metal artifacts from hip prostheses on CT images of the pelvis: value of iterative reconstructions. *Radiology, **268**: 237– 244*.
18. Maerz M, Mittermair P, Krauss A, *et al.* (2016) Iterative metal artifact reduction improves dose calculation accuracy. *Strahlentherapie und Onkologie*, ***192**: 403–13*.
19. Guilfoile C, Rampant P, House M (2017) The impact of smart metal artefact reduction algorithm for use in radiotherapy treatment planning. *Australasian Physical & Engineering Sciences in Medicine, **40**: 385– 94*.
20. Jeong S, Kim SH, Hwang EJ, *et al.* (2015) Usefulness of a metal artifact reduction algorithm for orthopedic implants in abdominal CT: Phantom and clinical study results. *American Journal of Roentgenology, **204**: 307-317*.
21. Jarriault AA and Lanaspeze C (2018) Assessment of smart MAR (Metal Artifact Reduction) algorithm for metallic artifact correction in external radiotherapy planning. *Physica Medica: European Journal of Medical Physics, **56** (1): 49*.
22. Katsura M, Sato J, Akahane M, *et al.* (2018) Current and Novel Techniques for Metal Artifact Reduction at CT: Practical Guide for Radiologists. *Radiographics, **38**(2): 450-461*.

[ Downloaded from ijrr.com on 2026-11-22 ]

[ DOI: 10.61186/ijrr.22.2.367 ]